ATR is required to complete meiotic recombination in mice

Sarai Pacheco[1,2], Andros Maldonado-Linares[1,2], Marina Marcet-Ortega[1,2], Cristina Rojas[1,2], Ana Martínez-Marchal[1,2], Judit Fuentes-Lazaro[1,2], Julian Lange[3,4], Maria Jasin[5], Scott Keeney[3,4], Oscar Fernández-Capetillo[6], Montserrat Garcia-Caldès[1,2] and Ignasi Roig[1,2,7]

[1]Genome Integrity and Instability Group, Institut de Biotecnologia i Biomedicina, Universitat Autònoma de Barcelona, Cerdanyola del Vallès, Spain.
[2]Department of Cell Biology, Physiology and Immunology, Universitat Autònoma de Barcelona, Cerdanyola del Vallès, Spain.
[3]Molecular Biology Program, Memorial Sloan Kettering Cancer Center, New York, New York, USA.
[4]Howard Hughes Medical Institute, Memorial Sloan Kettering Cancer Center, New York, New York, USA.
[5]Developmental Biology Program, Memorial Sloan Kettering Cancer Center, New York, New York, USA.
[6]Genomic Instability Group, Spanish National Cancer Research Centre, Madrid 28029, Spain.
[7]Correspondence should be addressed to I.R. (e-mail: ignasi.roig@uab.cat)

ABSTRACT

Precise execution of recombination during meiosis is essential for forming chromosomally balanced gametes. Meiotic recombination initiates with the formation and resection of DNA double-strand breaks (DSBs). Binding of replication protein A (RPA) at resected DSBs fosters association of RAD51 and DMC1, the primary effectors of homology search. It is well appreciated that cellular responses to meiotic DSBs are critical for efficient repair and quality control, but molecular features of these responses remain poorly understood, particularly in mammals. Here we provide evidence that the DNA damage response protein kinase ATR is crucial for meiotic recombination and completion of meiotic prophase in mice. Using a hypomorphic *Atr* mutation and pharmacological inhibition of ATR *in vivo* and in cultured spermatocytes, we show that ATR, through its effector kinase CHK1, promotes efficient RAD51 and DMC1 assembly at RPA-coated DSB sites and establishment of interhomolog connections during meiosis. Furthermore, our findings suggest that ATR promotes local accumulation of recombination markers on unsynapsed axes during meiotic prophase to favor homologous chromosome synapsis. These data reveal that ATR plays multiple roles in mammalian meiotic recombination.

INTRODUCTION

During the first meiotic division, hundreds of programmed DNA double-strand breaks (DSBs) are formed throughout the genome by the SPO11 protein[1]. The repair of these lesions by homologous recombination promotes homologous chromosome synapsis and crossover formation. Crossovers are essential for proper chromosome segregation and thus for preventing aneuploidy in gametes[2].

The cellular machinery that senses meiotic DSBs and regulates their repair is similar to the surveillance proteins that monitor DNA integrity in somatic cells and that, as a result of DNA damage, activate repair pathways, arrest cell cycle progression, and, if necessary, induce apoptosis[3,4]. A major one of these regulators in mice is the ataxia telangiectasia mutated and Rad-3 related (ATR) protein kinase[3,4]. ATR is activated by the presence of single-stranded DNA (ssDNA), which mainly arises from stalled replication forks or resected DSBs. ssDNA is rapidly covered by the ssDNA-binding protein complex RPA, which recruits ATR and its cofactors. ATR activation promotes stabilization and restart of stalled replications forks, DNA repair, and cell cycle arrest[3].

In mammalian meiosis, ATR accumulates on unsynapsed chromosome axes, such as the heterologous parts of the X and Y chromosomes[5]. This accumulation causes chromatin alterations that, in males, condense the sex chromosomes into a distinct chromatin domain known as the sex body. Such heterochromatinization leads to the transcriptional silencing of these regions, referred to as meiotic sex chromosome inactivation (MSCI)[6]. MSCI is indispensable for the completion of meiotic prophase, as sex-body failure provokes a mid-prophase arrest[7]. Although DSBs may contribute to this mode of ATR action, DSB formation is not strictly required as ATR can promote a similar response to unsynapsed axes in the absence of meiotic DSBs[8,9].

Whether ATR also functions in response to meiotic DSBs has remained obscure. In yeast, the ATR ortholog Mec1 is involved in directing meiotic cell cycle progression, promoting meiotic recombination, and controlling crossover formation[10]. In plants, ATR also promotes meiotic recombination by regulating recombinase DMC1 deposition at resected DSBs[11]. In mouse spermatocytes, ATR and its cofactors co-localize with other DNA repair proteins at sites undergoing homologous recombination, suggesting that ATR functions in meiotic recombination[12]. However, this hypothesis has not been formally tested, in part because abolition of *Atr* expression is embryonically lethal[13]. We overcame this challenge in this study by diminishing ATR function using genetic and pharmacological tools. Our findings revealed previously invisible functions for ATR in proper loading of strand-exchange proteins at DSBs, correct timing of crossover formation, formation of the synaptonemal complex (SC, the zipper-like proteinaceous structure that juxtaposes homologous chromosomes), and proper accumulation of recombination markers on the axes of unsynapsed chromosomes.

RESULTS

Using the Seckel mouse model to study ATR function in meiosis

We used a previously described hypomorphic mutation that reduces ATR expression in most tissues[14]. This allele mimics a mutation found in some human patients with Seckel syndrome (OMIM 210600), which is characterized by dwarfism, microcephaly, mental retardation and a beak-like nose[15]. The mutation is a synonymous A to G transition in exon 9 that causes frequent skipping of this exon during splicing, thereby severely reducing *Atr* expression[14,16]. In male mice homozygous for this "Seckel" allele (Atr^{S}), whole-testis *Atr* mRNA levels were substantially reduced (**Fig. 1a**). Testes from adult $Atr^{S/S}$ mice were much smaller than wild type (26.0% ± 11.1% of wild type, at 2–4 months of age, mean ± SD, N=20). This difference may be attributable to the dwarfism phenotype of Seckel mice[14] rather than a meiotic arrest. Indeed, the cellular composition of the seminiferous tubules appeared grossly normal (**Supplementary Fig. 1a**) and a previous study found that $Atr^{S/S}$ mice produce functional sperm[14].

Meiotic prophase stages of surface-spread spermatocytes can be determined by the cytological patterns of axis and SC components. At leptonema, SYCP3 protein begins to form the axis of each chromosome (**Supplementary Fig. 1b**). Synapsis begins at zygonema and leads to the formation of the SC containing SYCP1. At pachynema, autosomal homologous chromosomes are fully synapsed and SYCP3 and SYCP1 proteins completely co-localize. At diplonema, SCs disassemble but homologous chromosomes remain held together by chiasmata. Cytological evaluation of $Atr^{S/S}$ germ cells revealed that both the total percent of cells in meiotic prophase and the fractions of meiotic cells within each prophase stage were similar to wild type (**Supplementary Fig. 1c**). Taken together, these results show that $Atr^{S/S}$ cells are capable of progressing through meiosis and completing spermatogenesis.

We sought evidence of reduced ATR function in $Atr^{S/S}$ spermatocytes. The only known meiotic role of ATR is in sex-body formation and MSCI at pachynema[5,7]. Since sex-body formation was indistinguishable in wild-type and Seckel mice (wild type: 0.4% ± 0.6%, N=318; $Atr^{S/S}$: 2.3% ± 1.2%, N=389; p=0.183, one-way ANOVA), we analyzed the localization pattern of ATR and the intensity of three ATR-dependent sex-body markers in pachytene $Atr^{S/S}$ spermatocytes (**Fig. 1b, c and Supplementary Fig. 1d**). ATR localizes to the unsynapsed axes of the sex chromosomes, where it phosphorylates the histone H2AX to form γH2AX[5]. With the help of MDC1, ATR spreads to the XY chromatin, where it continues to phosphorylate H2AX[17]. Finally, other sex-body markers such as SUMO-1 are incorporated into the XY chromatin[17]. In wild type, most cells contained ATR localized to both the chromatin and the axes of the sex chromosomes. In contrast, most $Atr^{S/S}$ cells displayed ATR only on the XY axes. In addition, for each of the three ATR-dependent sex-body markers (γH2AX, MDC1 and SUMO-1), we observed a significant change in total signal intensity in $Atr^{S/S}$ compared with wild type. Notably, although most $Atr^{S/S}$ cells lacked ATR in XY chromatin, we detected the other three sex-body markers there. Signal intensities of γH2AX and SUMO-1 were reduced as expected, but MDC1 signal was higher, possibly reflecting a compensatory mechanism endeavoring to promote ATR translocation into XY chromatin. Despite these alterations, MSCI appears to be unaffected, as the X-linked gene *Zfx* was efficiently silenced in pachytene-stage $Atr^{S/S}$ spermatocytes (**Supplementary Fig. 1e, f**). We conclude that wild-type levels of ATR function are not needed to initiate and/or maintain MSCI. Importantly, however, our findings demonstrate that the reduced *Atr* expression in Seckel mice causes mild changes in ATR function in spermatocytes.

Seckel mouse spermatocytes display modest meiotic recombination defects

$Atr^{S/S}$ cells displayed subtle recombination defects. First, while analyzing γH2AX staining of the sex body, we detected persistent autosomal γH2AX patches in pachytene spermatocytes. During early prophase of meiosis, histone H2AX is phosphorylated by ATM in response to

meiotic DSBs, which are repaired as prophase progresses[8,18,19]. In control mice, autosomal γH2AX progressively disappeared during prophase (**Fig. 1d**). From pachynema onwards, γH2AX was mostly confined to the sex body, but a few γH2AX patches were visible on the autosomes, presumably at remaining unrepaired DSB sites. In *Atr*$^{S/S}$ spermatocytes, the numbers of autosomal γH2AX patches at early pachynema, late pachynema and diplonema were higher than in wild type (**Fig. 1e**), suggesting delayed repair kinetics.

Second, whereas autosomal synapsis was indistinguishable in *Atr*$^{S/S}$ and control spermatocytes, we detected impaired sex-chromosome synapsis in *Atr*$^{S/S}$ cells (**Supplementary Fig. 1b**). Since the XY pair is almost completely heterologous except for the small pseudoautosomal region (PAR), sex-chromosome synapsis must be mediated by DSBs occurring within the PAR[20]. Two-fold more *Atr*$^{S/S}$ spermatocytes displayed unsynapsed sex chromosomes at pachynema than control cells (12.2% in *Atr*$^{+/+}$ (N=197) vs. 25.1% in *Atr*$^{S/S}$ (N=235), p=0.0013, Fisher's exact test).

To further investigate ATR function in meiotic recombination, we examined RAD51 and DMC1, which associate with resected DSBs and catalyze strand exchange[21,22]. We quantified these markers at progressive stages of meiotic prophase (**Fig. 2a,b, Supplementary Table 1**). In wild type, RAD51 and DMC1 foci were most abundant at leptonema, then progressively decreased through diplonema, when most foci localized to the non-homologous portions of the sex chromosomes. RAD51 and DMC1 focus numbers were higher in pachtyene *Atr*$^{S/S}$ spermatocytes than in wild-type controls, consistent with the γH2AX results. In leptonema through zygonema, in contrast, fewer foci were observed in the mutant. Thus, there appear to be temporally distinct defects in recombination in the *Atr*$^{S/S}$ spermatocytes.

The reduced focus counts in early spermatocytes could reflect either a deficiency in the formation or early processing of DSBs, or defective loading of RAD51 and DMC1. To distinguish between these possibilities, we examined early steps of DSB formation and processing. First, we studied whole-testis DSB levels in *Atr*$^{S/S}$ mice by analyzing SPO11-oligonucleotide complexes, which are a direct readout of SPO11 function[23]. Unlike other mouse mutants with small testes[24–26], *Atr*$^{S/S}$ mice do not display prophase arrest, so the cellular composition (i.e., fractions of cell types) of their testes is similar to wild type (**Supplementary Fig. S1a-c**). Thus, to account for the dwarfism of Seckel mice[14], we compared SPO11-oligonucleotide signal in *Atr*$^{S/S}$ with wild type after normalization by testis weight. By this measure, we did not observe a reduction in SPO11 activity in *Atr*$^{S/S}$ testes; if anything, testis-weight-normalized SPO11-oligonucleotide levels were slightly elevated in mutant testes (1.6 ± 0.5 fold, mean ± SD, N=2) (**Fig. 2d**). These findings suggest that SPO11-induced DSB numbers are not reduced in *Atr*$^{S/S}$ spermatocytes.

Second, we examined the formation of RPA foci, which decorate ssDNA at resected DSB sites prior to the loading of RAD51 and DMC1[21]. In control spermatocytes, RPA focus numbers peaked in zygonema, then progressively decreased (**Fig. 2c, Supplementary Table 1**). RPA focus counts in *Atr*$^{S/S}$ spermatocytes were elevated at early leptonema. A straightforward interpretation of the altered RPA, RAD51, and DMC1 focus numbers is that RPA tends to persist longer at DSB sites in *Atr*$^{S/S}$ cells because of impaired loading of RAD51 and DMC1.

Physical linkages (chiasmata) between homologous chromosomes are crucial for accurate chromosome segregation at metaphase I. At least one crossover per bivalent is required to ensure proper orientation on the first meiotic spindle[27]. Because yeast Mec1 participates in controlling the number and distribution of crossovers[28,29], we investigated crossover formation in Seckel spermatocytes. In mice, the MLH1 protein is required for formation of the majority (~90%) of crossovers and it cytologically marks most crossover-designated sites at pachynema[30]. Pachytene *Atr*$^{S/S}$ spermatocytes displayed one less MLH1 focus on average than controls (**Fig. 3a**), attributable to a significant increase in the number of

autosomal bivalents lacking an MLH1 focus (**Fig. 3b**). However, we detected no difference in the number of achiasmate autosomal bivalents at diplonema (**Fig. 3c**). These data may indicate that MLH1 focus formation is delayed in *Atr*$^{S/S}$ cells or that ATR regulates the number of crossovers that are repaired by MLH1-dependent and -independent pathways.

Crossover control mechanisms regulate not only the number of crossover events but also their location[31]. The presence of one crossover inhibits the occurrence of another in its vicinity by a mechanism known as interference, which leads to a non-random distribution of crossovers[31,32]. We asked whether ATR reduction affected the distribution of MLH1 foci. We found a similar distribution along autosomal SCs in *Atr*$^{S/S}$ and wild type (**Fig. 3d**). In addition, the strength of cytological interference quantified using the gamma distribution[32] showed similar interference in both genotypes (**Fig. 3e**). Thus, although wild-type ATR levels are required for proper MLH1 focus numbers at pachynema, focus distribution is not substantially altered in *Atr*$^{S/S}$ cells.

ATR inhibition *in vivo* impairs meiotic recombination

Seckel mice do not completely abolish *Atr* expression (**Fig. 1a**) and they express a truncated ATR isoform that may not be functionally inert[14]. Thus, to further assess the role of ATR in meiotic recombination, we established an experimental system to chemically inhibit ATR. AZ20 is a selective ATR inhibitor (ATRi) that has been developed as a potential anti-cancer drug[33]. It inhibits ATR function *in vitro* and in cell culture systems, and its oral administration to mice carrying xenografted adenocarcinoma cells reduces tumor growth[33].

Wild-type adult males were dosed orally with AZ20 or vehicle solution (DMSO) for three days, the length of time normally required for a spermatocyte that initiates meiosis to complete homologous chromosome synapsis *in vivo*[34]. In control mice, 13.3% of testis cells were SYCP3-positive; of these, 81.5% were in pachynema or diplonema (**Fig. 4a,b**). AZ20-treated mice had fewer SYCP3-positive spermatocytes and altered proportions of prophase stages, including an increased fraction of zygotene cells ($p<0.0001$, Fisher's exact test) and an almost complete loss of diplotene cells ($p<0.0001$, Fisher's exact test, see below) (**Fig. 4a,b**). We analyzed sex-body formation, judged by γH2AX deposition on the XY chromatin of pachytene cells, as a readout of ATR function. Compared with controls, AZ20-treated mice had 13-fold more pachytene cells lacking a sex body (DMSO: 0.25% ± 0.35%, N=400; AZ20: 3.25% ± 0.35%, N=400; Mean ± SD, $p=0.014$, one-way ANOVA, **Fig. 4d**). These data indicate that *in vivo* treatment with AZ20 inhibits ATR activity in meiosis and that this inhibition affects meiotic progression.

Next, we analyzed sex-chromosome synapsis and recombination markers. Similar to results with *Atr*$^{S/S}$ mice, AZ20 treatment caused a more than two-fold increase in the frequency of unsynapsed sex chromosomes at pachynema (**Fig. 4c**). AZ20-treated spermatocytes exhibited fewer RAD51 foci during leptonema and early zygonema, and, as observed in *Atr*$^{S/S}$ spermatocytes, the decrease in RAD51 focus number was accompanied by a significant increase in the number of RPA foci at early leptonema (**Fig. 4e , Supplementary Table 2**). These results suggest that RAD51 association with resected DSBs is delayed in spermatocytes from AZ20-treated males, which could in turn affect sex chromosome synapsis.

To corroborate the ATR role in the formation of MLH1 foci, we treated adult males with AZ20 or DMSO for 7 days, the time required for a leptotene spermatocyte to reach mid/late-pachynema, where MLH1 foci can be analyzed. This longer treatment resulted in a slightly reduced percentage of SYCP3-positive spermatocytes and an increased number of apoptotic cells per tubule (**Fig. 4a,b,f**). The prolonged treatment resulted similarly in a large increase in the fraction of pachytene spermatocytes lacking a sex body (DMSO: 0.5% ± 0.7%, N=200; AZ20-treated: 14.5% ± 0.7%, N=200, Mean ± SD, $p=0.0002$, one-way ANOVA). Importantly, treated mice lacked diplotene spermatocytes (**Fig. 4b**), in agreement with a previous report that ATR function is required to exit pachynema[5]. ATRi-treated pachytene spermatocytes displayed, on average, one less MLH1 focus than control spermatocytes (**Fig. 4g**). The lack of diplotene

spermatocytes in ATRi-treated samples precluded study of achiasmate bivalents. As in *Atr*$^{S/S}$ spermatocytes, the distribution of MLH1 foci was not substantially altered in ATRi-treated spermatocytes and MLH1 interfocal distances displayed positive interference (**Fig. 4h, i**). Furthermore, modeling interfocal distances to a gamma distribution gave lower (figure says higher, but I don't think this is right) values of cytological interference than the controls, but within the range considered normal in other studies[19,32].

In sum, the results from *in vivo* treatment of wild-type mice recapitulate our findings with the Seckel mouse model, with some differences that can be attributed to a greater decrease in ATR function in AZ20-treated spermatocytes. Specifically, unlike *Atr*$^{S/S}$ mice, AZ20-treated samples displayed meiotic prophase arrest and more severe alterations to recombination marker focus counts (**Supplementary Tables 1 and 2**). Also, whereas almost all pachytene *Atr*$^{S/S}$ spermatocytes displayed a sex body 15% of 7-day AZ20-treated pachytene spermatocytes did not. Thus, reduced ATR activity may prevent sex-body formation, which would cause pachytene arrest and an increase in apoptosis in AZ20-treated samples. Moreover, we showed previously that abnormal accumulation of ATR on the XY pair may be sufficient to phosphorylate H2AX but insufficient to implement the silencing of these chromosomes[35]. Thus, we postulate that the arrest observed after *in vivo* treatment with AZ20 may be the consequence of a failure to silence the sex chromosomes at pachynema.

ATR inhibition in culture affects meiotic prophase progression and recombination

Although AZ20 treatment appeared to attenuate ATR activity more than the Seckel mutation did, the accumulation of γH2AX on the XY chromatin in most treated spermatocytes indicated that ATR function was not fully blocked. This could be attributable to the blood-testis barrier, which controls entry of molecules from circulating blood into the seminiferous tubules[36]. Thus, we cultured fragments of neonatal testes in media containing AZ20. We hypothesized that this strategy could surmount the blood-testis barrier, thereby increasing exposure of spermatocytes to AZ20 and better inhibiting ATR function.

We cultured testis fragments isolated from 5 days *post partum* (dpp) wild-type mice. Because ATR inhibition can interfere with DNA replication[37], fragments were initially cultured without treatment for 7 days to allow entry into meiosis. Then, for a further 7 days, fragments were cultured either without treatment or in the presence of different doses of AZ20 (0.2 μM, 1 μM or 5 μM) or equivalent volumes of DMSO (DMSO1, DMSO2 or DMSO3).

We used SYCP3 to assess meiotic prophase initiation, progression and synapsis. At day zero (D0, i.e., prior to culture), only 1% of testis cells were SYCP3-positive and were thus judged to be spermatocytes (**Fig. 5a,b**). After the initial 7 days of culture (D7), 13% of testis cells were spermatocytes, of which 75% were at leptonema. After two weeks of culture (D14), 16% of testis cells from untreated samples showed SYCP3 staining. Importantly, 25% of these D14 spermatocytes displayed complete synapsis consistent with having reached pachynema. A low dose of AZ20 had no effect on meiotic progression: at D14, proportions of spermatocytes at different prophase stages were indistinguishable between 0.2 μM AZ20-treated, DMSO1-treated and untreated samples (**Fig. 5a-d**). However, at higher doses (1 μM or 5 μM), cultured samples exhibited a decreased fraction of SYCP3-positive cells compared with DMSO-treated controls, suggesting that some spermatocytes had died between D7 and D14. We did not detect any spermatocytes with complete synapsis or with a sex body (**Fig. 5c-e, Supplementary Table 3**).

We used 5 μM AZ20-treated samples to evaluate whether recombination defects observed in the *in vivo* models were recapitulated *in vitro*. Whereas untreated and DMSO3 samples exhibited similar RAD51 focus dynamics, dramatically fewer foci were observed in 5 μM AZ20-treated samples (**Fig. 5f,g, Supplementary Table 4**). A severe effect on DMC1 focus formation was likewise seen (**Fig. 5h**). Similar to the *in vivo* models, RPA focus counts at early leptonema were higher from 5 μM AZ20-treated samples than in controls (**Fig. 5i, Supplementary Table 4**). DMSO treatment alone appeared to cause modest changes, as

fewer RPA foci were observed in late leptotene and late zygotene spermatocytes in DMSO3 samples compared with untreated, possibly due to DMSO toxicity (**Fig. 5i**). Nonetheless, ATRi-treated samples behaved differently from DMSO3-treated samples at all prophase stages. These data show that inhibition of ATR function alters RAD51 and DMC1 loading.

CHK1 function is required for proper RAD51 loading and meiotic prophase progression

Checkpoint kinase 1 (CHK1) is the major effector of the ATR signaling pathway[3]. In somatic cells ATR activates CHK1, which interacts with and phosphorylates RAD51 to promote repair of DNA lesions[3,38]. To investigate the effect of CHK1 perturbation on meiotic recombination, we targeted CHK1 protein *in vitro* with two specific inhibitors, PF-477736[39] and LY2603618[40] (referred to as CHK1i). As above, we cultured 5 dpp testis fragments for 7 days before subjecting them to CHK1i for an additional 7 days.

As assessed by SYCP3 immunostaining at D14, CHK1i-treated samples displayed fewer SYCP3-positive spermatocytes than DMSO-treated controls and no spermatocytes that had completed synapsis (**Fig. 5c**). Moreover, RAD51 focus numbers were substantially reduced, indicating that RAD51 loading onto chromosome axes was severely compromised (**Fig. 5j,k**). We conclude that disruption of the ATR-CHK1 pathway affects loading of RAD51 onto resected DSBs and restricts progression through meiotic prophase.

ATR promotes SC elongation

The absence of spermatocytes with complete SC formation after *in vitro* ATRi and CHK1i (**Fig. 5c-e, Supplementary Table 3**) suggested that ATR may participate in SC formation and/or elongation. We used a *Spo11* mutant to study how *in vivo* inhibition of ATR affected SC formation and/or elongation in the absence of meiotic recombination[41]. *Spo11*$^{-/-}$ spermatocytes fail to form DSBs but still form stretches of SC, so SC formation is independent of meiotic recombination in this genetic background. AZ20-treated *Spo11*$^{-/-}$ spermatocytes displayed the same number of SC stretches per cell as untreated *Spo11*$^{-/-}$ cells (**Supplementary Fig. 2a,b**). However, the average length of these fragments was shorter in ATRi-treated spermatocytes (**Supplementary Fig. 2a,c**). These findings suggest that wild-type levels of ATR function are not required for SC initiation but play a role in SC elongation.

ATR is required for the proper accumulation of recombination markers on unsynapsed chromosome axes

In yeast, Mec1 regulates meiotic recombination partner choice by phosphorylating Hop1[42,43] , the ortholog of mouse HORMA domain-containing protein HORMAD1, HORMAD1 is involved in several meiotic processes, localizes to chromosome axes at the onset of meiosis and becomes phosphorylated during meiotic progression[44,45] (discussed further below). In mouse, unsynapsed chromosomes tend to accumulate recombination markers during zygonema[46–49], implying that DSBs are continuously formed and processed in unsynapsed regions until the homolog is engaged for repair. Because ATR decorates unsynapsed axes in mice[5], where HORMAD1 accumulates, we asked whether ATR plays a role in DSB formation and early processing specifically in unsynapsed regions.

The X chromosome normally remains completely unsynapsed throughout zygonema[40], so it is a useful model for examining the kinetics of recombination markers on unsynapsed axes. We scored RAD51 and RPA focus density on the X chromosome at early and late zygonema in wild-type and *Atr*$^{S/S}$ spermatocytes (**Fig. 6a-d**). The densities of RAD51 and RPA foci in wild type were higher in late zygonema than early zygonema ($p=0.0005$ for RAD51 and $p=0.023$ for RPA, t test) (**Fig. 6a-d**), as previously reported[46]. In *Atr*$^{S/S}$ spermatocytes in contrast, neither RAD51 focus density, which was substantially lower at both sub-stages, nor RPA focus density rose significantly as zygonema progressed ($p>0.05$, t test) (**Fig. 6a-d**).

To corroborate these findings, we asked whether culturing testis fragments in 5 μM AZ20 also curtailed accumulation of recombination markers on unsynapsed chromosomes (**Fig. 6e**). Indeed, AZ20-treated samples exhibited a significant decrease in the density of RPA foci on unsynapsed axes as zygonema progressed ($p=0.0004$, t test). Similar to our earlier observations for total RPA counts, DMSO treatment affected RPA focus density on unsynapsed axes, but ATRi-treatment further reduced this density. These findings indicate that ATR contributes to the normal patterns of accumulation of recombination markers on unsynapsed chromosome axes.

DISCUSSION

In this study, we used a combination of genetic and pharmacological tools to examine the function of ATR in meiotic recombination. This strategy is a useful approach for studying the meiotic role(s) of a protein whose null mutation is embryonically lethal. Although conditional models can also address this issue, the use of specific inhibitors is advantageous because mice of desired genotypes are more readily obtained when studying a single locus. This aspect significantly reduces the number of mice required to perform the study.

Using this approach, we were able to inhibit ATR function to different degrees, as determined by meiotic prophase progression and sex-body formation. ATR is known to be required to form the sex body[5]. Upon *in vitro* administration of ATRi, spermatocytes were blocked by zygonema (i.e., prior to sex-body formation), so we infer that this condition delivered the strongest inhibition. *In vivo* administration of ATRi allowed accumulation of pachytene spermatocytes, thus inhibition was not as strong as in the *in vitro* setting. Finally, $Atr^{S/S}$ spermatocytes displayed grossly normal meiotic progression and nearly wild-type levels of sex-body formation. Of note, markers of other meiotic processes (e.g., RAD51 focus counts and XY synapsis) were also more perturbed in AZ20-treated samples than in $Atr^{S/S}$ mice.

Our data show that ATR and its effector CHK1 play a critical role in the loading of RAD51 and DMC1 onto chromatin. While RAD51 focus numbers were reduced in $Atr^{S/S}$ spermatocytes relative to wild type only at early leptonema, DMC1 focus numbers were significantly lower from early leptonema through late zygonema. As expected from previous studies performed in other model organisms and mammals[50,51],the different effects on the kinetics of RAD51 and DMC1 foci corroborate that these recombinases are regulated differently. Distinct regulation may be attributable to several factors. First, while the protein sequences of mouse RAD51 and DMC1 are very similar (53.3% identical and 64% similar), they differ at a residue that may be critical for RAD51 activity. In mammalian somatic cells, RAD51 Threonine 309 is phosphorylated by CHK1 upon activation of ATR by RPA-coated DNA structures, and this post-translational modification promotes RAD51 focus assembly[38]. It has been suggested that CHK1-dependent RAD51 phosphorylation is required for RAD51 to displace RPA from resected DSB ends and initiate homology search[38]. The paralogous residue in DMC1 is Leucine 310, hence it cannot be similarly regulated. Second, the current favored model of RAD51 and DMC1 loading onto resected DSBs in meiosis proposes that RAD51 loading is a prerequisite for the incorporation of DMC1[50]. Thus, this interdependency could also account for the more severe effect on DMC1 focus formation observed in ATR-defective spermatocytes.

Aberrant loading and kinetics of RAD51 and DMC1 may have implications for homologous chromosome pairing and synapsis. Cytologically, the phenotype of ATR-deficient spermatocytes (altered kinetics of recombination markers, reduced number of MLH1 foci at pachynema, increased proportion of spermatocytes at zygonema, and defects in sex-chromosome synapsis) is consistent with impaired meiotic recombination. However, our data in the DSB-deficient $Spo11^{-/-}$ background indicate that ATR can also promote SC extension independently of its role in meiotic recombination. Several proteins of the chromosome axis, including HORMAD1, are phosphorylated during meiotic prophase[52]. HORMAD1 is required for normal numbers of meiotic DSBs, proper SC formation and recruitment of ATR onto unsynapsed chromosome axes[53]. At the onset of meiotic prophase HORMAD1 is localized at the chromosome axes[44]. As a result of DSB formation, HORMAD1 is phosphorylated, presumably by ATR[5,52], and when homologous chromosomes synapse, HORMAD1 is displaced from the axes. Thus, we hypothesize that the role of ATR in SC elongation may be mediated by HORMAD1. Indeed, the yeast HORMAD1 ortholog Hop1 is phosphorylated by Mec1 and Tel1 (the orthologs of ATR and ATM), and this phosphorylation promotes SC formation[42].

In budding yeast, Mec1 participates in two additional key aspects of meiotic recombination. First, it biases recombination towards the homologous chromosome over the

sister chromatid as the preferred template for meiotic DSB repair[43]. Second, it indirectly promotes DSB formation during meiotic prophase by inhibiting the transcription factor Ndt80, which is required to exit pachynema and thereby close the cell cycle window during which Spo11 forms DSBs[54]. In yeast, inter-sister meiotic recombination is over three times faster than inter-homolog recombination[42]. If ATR participates similarly in the implementation of inter-homolog bias in mouse, ATR-deficient spermatocytes might repair DSBs more rapidly by recombination between sister chromatids. This model could explain the observed reduction in recombination marker density on unsynapsed axes at zygonema. In support of this model, the reduction in RPA foci at zygonema in *Atr*$^{S/S}$ spermatocytes despite globally unaltered DSB numbers could reflect a more rapid turnover of recombination markers by inter-sister repair. However, our data also provide results that seem inconsistent with this interpretation. The increase in recombination markers (γH2AX, RAD51 and DMC1) on the synapsed axes of pachytene-stage *Atr*$^{S/S}$ spermatocytes appears difficult to reconcile with faster repair by inter-sister recombination. However, it is also plausible that ATR may play another role in DSB repair from mid/late pachynema onwards. It has been proposed that DSB repair processes other than canonical meiotic recombination may be active from mid pachynema onwards[18], including non-homologous end joining (NHEJ)[55]. Spermatocytes from mice deficient for KU70, which is required for NHEJ, present more γH2AX patches at late pachynema and diplonema than control cells, suggesting that NHEJ participates in DSB repair at late meiotic prophase[55].Thus, the accumulation of γH2AX patches observed at mid/late pachynema and diplonema in Seckel mice could also reflect that ATR is required to activate alternative DSB repair pathway(s) at later stages of meiotic prophase.

Finally, the presence of normal numbers of achiasmate bivalents at diplonema in Seckel mouse spermatocytes suggests that, ATR function in that context is sufficient for normal levels of crossover formation. We did not observe enough *in vivo* AZ20-treated diplotene spermatocytes to study chiasma formation when ATR function is further reduced. Nonetheless, our data show that ATR function is required for the proper number of MLH1 foci at pachynema.

In summary, our data show that the ATR-CHK1 pathway is required for the completion of meiotic recombination in mammalian spermatocytes. RAD51 and DMC1 kinetics are altered when ATR or CHK1 function is abrogated, suggesting a role for this pathway in loading RAD51 and DMC1 onto resected DSBs. Furthermore, deficiency in ATR function affects SC formation and the accumulation of recombination markers along unsynapsed axes during zygonema. Thus, reduction in ATR function may impair the ability of homologous chromosomes to pair and synapse during meiotic prophase. Finally, our finding that *in vivo* exposure to AZ20 causes meiotic prophase arrest is relevant when considering the use of ATR inhibitors in cancer therapy, since meiotic arrest may result in infertility. Further studies should be performed to determine how long this arrest lasts after exposure to the drug.

ACKNOWLEDGMENTS

We thank M. A. Handel (The Jackson Laboratory, Bar Harbor, USA) for the anti-H1T antibody; E. Marcon for the anti-RPA antibody (University of Toronto, Canada); J. Turner (National Institute for Medical Research, London, UK) for assistance in the RNA-FISH experiments, for the X chromosome probe and for sharing unpublished data; L. Kauppi (University of Helsinki, Finland) for providing us with protocols for the testis cultures; and members of the Roig lab and the Spanish Ministerio de Ciencia e Innovación-funded Network of Spanish groups working on Meiosis (MeioNet, BFU2015-71786-REDT) and Enrique Martínez Pérez (Imperial College, London, UK) for helpful discussions. MMO was supported by a FPI fellowship from the Ministerio de Ciencia e Innovación (BES-2011-045381). JL was supported in part by American Cancer Society post-doctoral fellowship (PF-12-157-01-DMC). SK is an Investigator of the Howard Hughes Medical Institute. This work was supported by the Ministerio de Ciencia e Innovación (BFU2010-18965, BFU2013-43965-P and BFU2016-80370-P, IR), by the UAB-Aposta award to young investigators (APOSTA2011-03, IR) and by the NIH (R01 GM105421, MJ and SK).

AUTHOR CONTRIBUTIONS

SP, MMO and IR conceived the experiments. OFC provided critical reagents. SP, AM, MMO, CR, AMM, JL and IR performed the experiments. SP, AM, MMO, JL, MJ, SK, OFC, MGC and IR analyzed the data. SP, JL and IR wrote the manuscript.

REFERENCES

1. Keeney, S., Giroux, C. N. & Kleckner, N. Meiosis-specific DNA double-strand breaks are catalyzed by Spo11, a member of a widely conserved protein family. *Cell* **88,** 375–84 (1997).

2. Baudat, F., Imai, Y. & de Massy, B. Meiotic recombination in mammals: localization and regulation. *Nat. Rev. Genet.* **14,** 794–806 (2013).

3. Cimprich, K. a & Cortez, D. ATR: an essential regulator of genome integrity. *Nat. Rev. Mol. Cell Biol.* **9,** 616–27 (2008).

4. Maréchal, A. & Zou, L. DNA damage sensing by the ATM and ATR kinases. *Cold Spring Harb. Perspect. Biol.* **5,** (2013).

5. Royo, H. *et al.* ATR acts stage specifically to regulate multiple aspects of mammalian meiotic silencing. *Genes Dev.* **27,** 1484–1494 (2013).

6. Burgoyne, P. S., Mahadevaiah, S. K. & Turner, J. M. a. The consequences of asynapsis for mammalian meiosis. *Nat. Rev. Genet.* **10,** 207–16 (2009).

7. Royo, H. *et al.* Evidence that meiotic sex chromosome inactivation is essential for male fertility. *Curr. Biol.* **20,** 2117–23 (2010).

8. Bellani, M. A., Romanienko, P. J., Cairatti, D. A. & Camerini-Otero, R. D. SPO11 is required for sex-body formation, and Spo11 heterozygosity rescues the prophase arrest of Atm-/- spermatocytes. *J. Cell Sci.* **118,** 3233–45 (2005).

9. Barchi, M. *et al.* Surveillance of Different Recombination Defects in Mouse Spermatocytes Yields Distinct Responses despite Elimination at an Identical Developmental Stage. **25,** 7203–7215 (2005).

10. Subramanian, V. V & Hochwagen, A. The Meiotic Checkpoint Network: Step-by-Step through Meiotic Prophase. *Cold Spring Harb. Perspect. Biol.* **6,** (2014).

11. Kurzbauer, M.-T., Uanschou, C., Chen, D. & Schlögelhofer, P. The recombinases DMC1 and RAD51 are functionally and spatially separated during meiosis in Arabidopsis. *Plant Cell* **24,** 2058–70 (2012).

12. Moens, P. B. *et al.* The association of ATR protein with mouse meiotic chromosome cores. *Chromosoma* **108,** 95–102 (1999).

13. Brown, E. J. & Baltimore, D. ATR disruption leads to chromosomal fragmentation and early embryonic lethality. *Genes Dev.* **14,** 397–402 (2000).

14. Murga, M. *et al.* A mouse model of ATR-Seckel shows embryonic replicative stress and accelerated aging. *Nat. Genet.* **41,** 891–8 (2009).

15. O'Driscoll, M. Mouse models for ATR deficiency. *DNA Repair (Amst).* **8,** 1333–7 (2009).

16. O'Driscoll, M., Ruiz-Perez, V. L., Woods, C. G., Jeggo, P. A. & Goodship, J. A. A splicing mutation affecting expression of ataxia-telangiectasia and Rad3-related protein (ATR) results in Seckel syndrome. *Nat. Genet.* **33,** 497–501 (2003).

17. Ichijima, Y. *et al.* MDC1 directs chromosome-wide silencing of the sex chromosomes in male germ cells. *Genes Dev.* **25,** 959–71 (2011).

18. Mahadevaiah, S. K. *et al.* Recombinational DNA double-strand breaks in mice precede synapsis. *Nat. Genet.* **27,** 271–6 (2001).

19. Barchi, M. *et al.* ATM promotes the obligate XY crossover and both crossover control and chromosome axis integrity on autosomes. *PLoS Genet.* **4,** e1000076 (2008).

20. Kauppi, L. *et al.* Distinct properties of the XY pseudoautosomal region crucial for male meiosis. *Science* **331,** 916–20 (2011).

21. Bannister, L. A. & Schimenti, J. C. Homologous recombinational repair proteins in mouse meiosis. *Cytogenet. Genome Res.* **107,** 191–200 (2004).

22. Brown, M. S., Grubb, J., Zhang, A., Rust, M. J. & Bishop, D. K. Small Rad51 and Dmc1 Complexes Often Co-occupy Both Ends of a Meiotic DNA Double Strand Break. *PLOS Genet.* **11,** e1005653 (2015).

23. Pan, J. & Keeney, S. Detection of SPO11-oligonucleotide complexes from mouse testes. *Methods Mol. Biol.* **557,** 197–207 (2009).

24. Pittman, D. L. *et al.* Meiotic prophase arrest with failure of chromosome synapsis in mice deficient for Dmc1, a germline-specific RecA homolog. *Mol. Cell* **1,** 697–705 (1998).

25. De Vries, S. S. *et al.* Mouse MutS-like protein Msh5 is required for proper chromosome synapsis in male and female meiosis. *Genes Dev.* **13,** 523–531 (1999).

26. Edelmann, W. *et al.* Meiotic pachytene arrest in MLH1-deficient mice. *Cell* **85,** 1125–34 (1996).

27. Moens, P. B., Marcon, E., Shore, J. S., Kochakpour, N. & Spyropoulos, B. Initiation and resolution of interhomolog connections: crossover and non-crossover sites along mouse synaptonemal complexes. *J. Cell Sci.* **120,** 1017–27 (2007).

28. Bartrand, A. J., Iyasu, D., Marinco, S. M. & Brush, G. S. Evidence of meiotic crossover control in Saccharomyces cerevisiae through Mec1-mediated phosphorylation of replication protein A. *Genetics* **172,** 27–39 (2006).

29. Serrentino, M.-E., Chaplais, E., Sommermeyer, V. & Borde, V. Differential association of the conserved SUMO ligase Zip3 with meiotic double-strand break sites reveals regional variations in the outcome of meiotic recombination. *PLoS Genet.* **9,** e1003416 (2013).

30. Anderson, L. K., Reeves, A., Webb, L. M. & Ashley, T. Distribution of crossing over on mouse synaptonemal complexes using immunofluorescent localization of MLH1 protein. *Genetics* **151,** 1569–79 (1999).

31. Berchowitz, L. E. & Copenhaver, G. P. Genetic interference: don't stand so close to me. *Curr. Genomics* **11,** 91–102 (2010).

32. De Boer, E., Stam, P., Dietrich, A. J. J., Pastink, A. & Heyting, C. Two levels of interference in mouse meiotic recombination. *Proc. Natl. Acad. Sci. U. S. A.* **103,** 9607–12 (2006).

33. Foote, K. M. *et al.* Discovery of 4-{4-[(3R)-3-Methylmorpholin-4-yl]-6-[1-(methylsulfonyl)cyclopropyl]pyrimidin-2-yl}-1H-indole (AZ20): a potent and selective inhibitor of ATR protein kinase with monotherapy in vivo antitumor activity. *J. Med. Chem.* **56,** 2125–38 (2013).

34. Goetz, P., Chandley, a C. & Speed, R. M. Morphological and temporal sequence of meiotic prophase development at puberty in the male mouse. *J. Cell Sci.* **65,** 249–63 (1984).

35. Pacheco, S. *et al.* The ATM Signaling Cascade Promotes Recombination-Dependent Pachytene Arrest in Mouse Spermatocytes. *PLOS Genet.* **11,** e1005017 (2015).

36. Mital, P., Hinton, B. T. & Dufour, J. M. The blood-testis and blood-epididymis barriers are more than just their tight junctions. *Biol. Reprod.* **84,** 851–8 (2011).

37. Toledo, L. I., Murga, M. & Fernandez-Capetillo, O. Targeting ATR and Chk1 kinases for cancer treatment: A new model for new (and old) drugs. *Mol. Oncol.* **5,** 368–373 (2011).

38. Sørensen, C. S. *et al.* The cell-cycle checkpoint kinase Chk1 is required for mammalian homologous recombination repair. *Nat. Cell Biol.* **7,** 195–201 (2005).

39. Blasina, A. *et al.* Breaching the DNA damage checkpoint via PF-00477736, a novel small-molecule inhibitor of checkpoint kinase 1. *Mol. Cancer Ther.* **7,** 2394–404 (2008).

40. Dai, Y. & Grant, S. New insights into checkpoint kinase 1 in the DNA damage response signaling network. *Clin. Cancer Res.* **16,** 376–83 (2010).

41. Baudat, F., Manova, K., Yuen, J. P., Jasin, M. & Keeney, S. Chromosome synapsis defects and sexually dimorphic meiotic progression in mice lacking Spo11. *Mol. Cell* **6,** 989–98 (2000).

42. Carballo, J. A., Johnson, A. L., Sedgwick, S. G. & Cha, R. S. Phosphorylation of the axial element protein Hop1 by Mec1/Tel1 ensures meiotic interhomolog recombination. *Cell* **132,** 758–70 (2008).

43. Grushcow, J. M. *et al.* Saccharomyces cerevisiae checkpoint genes MEC1, RAD17 and RAD24 are required for normal meiotic recombination partner choice. *Genetics* **153,** 607–20 (1999).

44. Wojtasz, L. *et al.* Mouse HORMAD1 and HORMAD2, two conserved meiotic chromosomal proteins, are depleted from synapsed chromosome axes with the help of TRIP13 AAA-ATPase. *PLoS Genet.* **5,** e1000702 (2009).

45. Daniel, K. *et al.* Meiotic homologue alignment and its quality surveillance are controlled by mouse HORMAD1. *Nat. Cell Biol.* **13,** 599–610 (2011).

46. Kauppi, L. *et al.* Numerical constraints and feedback control of double-strand breaks in mouse meiosis. *Genes Dev.* **27,** 873–86 (2013).

47. Thacker, D., Mohibullah, N., Zhu, X. & Keeney, S. Homologue engagement controls meiotic DNA break number and distribution. *Nature* **510,** 241–6 (2014).

48. Roig, I. *et al.* Mouse TRIP13/PCH2 is required for recombination and normal higher-order chromosome structure during meiosis. *PLoS Genet.* **6,** (2010).

49. Keeney, S., Lange, J. & Mohibullah, N. Self-organization of meiotic recombination initiation: general principles and molecular pathways. *Annu. Rev. Genet.* **48,** 187–214 (2014).

50. Brown, M. S. & Bishop, D. K. DNA Strand Exchange and RecA Homologs in Meiosis. *Cold Spring Harb. Perspect. Biol.* **7,** (2014).

51. Dai, J., Voloshin, O., Potapova, S. & Camerini-Otero, R. D. Meiotic Knockdown and Complementation Reveals Essential Role of RAD51 in Mouse Spermatogenesis. *Cell Rep.* **18,** 1383–1394 (2017).

52. Fukuda, T. *et al.* Phosphorylation of chromosome core components may serve as axis marks for the status of chromosomal events during mammalian meiosis. *PLoS Genet.* **8,** e1002485 (2012).

53. Daniel, K. *et al.* Meiotic homologue alignment and its quality surveillance are controlled by mouse HORMAD1. *Nat. Publ. Gr.* **13,** 599–610 (2011).

54. Gray, S., Allison, R. M., Garcia, V., Goldman, A. S. H. & Neale, M. J. Positive regulation of meiotic DNA double-strand break formation by activation of the DNA damage checkpoint kinase Mec1(ATR). *Open Biol.* **3,** 130019 (2013).

55. Ahmed, E. A., Sfeir, A., Takai, H. & Scherthan, H. Ku70 and non-homologous end joining protect testicular cells from DNA damage. *J. Cell Sci.* **126,** (2013).

56. Roig, I. *et al.* Female-specific features of recombinational double-stranded DNA repair in relation to synapsis and telomere dynamics in human oocytes. *Chromosoma* **113,** 22–33 (2004).

57. Mahadevaiah, S. K., Costa, Y. & Turner, J. M. A. Using RNA FISH to study gene expression during mammalian meiosis. *Methods Mol. Biol.* **558,** 433–44 (2009).

58. Lange, J. *et al.* ATM controls meiotic double-strand-break formation. *Nature* **479,** 237–40 (2011).

59. Sato, T. *et al.* In vitro production of functional sperm in cultured neonatal mouse testes. *Nature* **471,** 504–7 (2011).

60. Inselman, A., Eaker, S. & Handel, M. A. Temporal expression of cell cycle-related proteins during spermatogenesis: Establishing a timeline for onset of the meiotic divisions. *Cytogenet. Genome Res.* **103,** 277–284 (2003).

MATERIALS AND METHODS

Mice and genotyping

The *Atr Seckel (Atr^S)* and *Spo11* alleles were generated previously[14,41]. Genotyping was performed by PCR of tail tip DNA using previously designed primers[14,41]. The *Atr^S* allele was maintained on a C57BV6-129/Sv mixed genetic background. Experiments were performed using two or more mutant animals and compared to littermate control mice. When appropriate littermate controls were unavailable, control animals were obtained from other litters of the same matings and at the same age. All animals were sacrificed using CO_2 euthanization methods. Experimental procedures conform to the protocol CEEAH 1091 (DAAM6395) approved by the Ethics Committee for Animal Experimentation of the Universitat Autònoma de Barcelona and the Catalan Government.

RNA expression analysis

RNA from mouse testes was extracted using the RNeasy Plus Mini kit (Qiagen). The SuperScript III One-Step RT-PCR Taq High Fidelity (Invitrogen) was used to synthesize cDNA and amplify *Atr* transcripts using previously designed primers[16].

Cytology, Immunostaining and FISH

Testes were dissected from mice at 2–3 months of age and were processed for cytology and histology, as previously described[48,56]. Briefly, for surface spreading procedures, the tunica albuginea was removed and seminiferous tubules were released and minced to obtain a single-cell suspension. Cells were treated with a hypotonic solution (0.1 M sucrose) and fixed in 1% paraformaldehyde in H_2O with 0.1% Triton X-100 for 2 h. Slides were washed in 0.4% Kodak Photo-Flo and air-dried. Immunostaining of surface spreads was performed using standard methods[35]. The following primary antibodies were used: rabbit anti-SYCP3 (Abcam) 1:200 dilution, mouse anti-SYCP3 (Abcam) 1:200 dilution, mouse anti-SYCP1 (Abcam) 1:400 dilution, mouse anti-γH2AX (Millipore) 1:200 dilution, guinea pig anti-H1T (kindly donated by Dr. Mary Ann Handel) 1:500 dilution, rabbit anti-ATR (Calbiochem) 1:100 dilution, mouse anti-SUMO-1 (Life Technologies) 1:100 dilution, sheep anti-MDC1 (AbdSerotech) 1:100 dilution, rabbit anti-RAD51 (Calbiochem) 1:100 dilution, rabbit anti-RPA (kindly donated by Dr. Edita Marcon) 1:100 dilution, and mouse anti-MLH1 (BD Bioscience) 1:50 dilution. Combined immunofluorescence/FISH was performed using a BAC probe RP24-204O18 (CHORI BACPAC library) labeled with digoxigenin to detect the X-linked *Scml2* gene. After immunostaining, slides were treated with a pre-warmed denaturation solution (70% formamide in 2% SSC, pH 7.2–7.4) for 20 min at 74°C, incubated in a humid chamber for 2.5 h at 65ºC with 100 µl of 1 M sodium thiocyanate, and immediately immersed in denaturation solution for 20 min at 74ºC. Slides were dehydrated in a series of ethanol solutions. 5 µl of probe was mixed with one volume of hybridization buffer (4× SSC, 50% dextran sulphate, 2 mg/ml BSA, 2 mM vanadyl ribonucleoside), denatured for 10 min at 75ºC and reannealed for 10 min at 37ºC. Slides were incubated with hybridization mix for 72 h at 37ºC. Slide post-hybridization treatments consisted of three washes for 5 min in washing solution (50% formamide, 2× SSC pH 7.2–7.4) at 45°C, three washes for 5 min in 2× SSC at 45°C, one immersion in 4× SSC, 0.1% Tween 20 at room temperature, one incubation for 30 min with blocking buffer (4× SCC, 4 mg/ml BSA, 0.1% Tween-20) at 37°C, one incubation for 1 h with 30 µl of digoxigenin detection solution (10% Anti-Digoxigenin-Fluorescein (ApopTag Plus Fluorescein In Situ Apoptosis Detection kit (Millipore)) in 4× SSC, 0.1% Tween 20) at 37°C, and three washes for 5 min in 4× SSC, 0.1% Tween 20 at room temperature. DAPI (4',6-diamidino-2-phenylindole) (Sigma) was used to stain the DNA.

RNA-FISH and immunofluorescence

RNA FISH was carried out using BAC probe bMQ-372M23 (Mouse bMQ BAC library) labeled with digoxigenin to detect the *Zfx* gene, as previously described[57]. Briefly, BAC-containing bacteria were grown in an overnight LB-Chloramphenicol culture at 37°C and a standard miniprep method was used to isolate BAC DNA. 2 µg of BAC DNA were labeled using DIG-Nick Translation Mix (Roche) and precipitated with Cot-1 DNA (Invitrogen) and salmon sperm DNA (Stratagene). Mouse testes were minced, then cells were treated with CSK buffer (100 mM NaCl, 300 mM sucrose, 3 mM MgCl2, 10 mM PIPES, 0.5% Triton X-100, 2 mM vanadyl ribonucleoside (New England Biolabs)) and fixed in 4% paraformaldehyde in PBS, and slides were dehydrated in a series of ethanol solutions. 30µl of probe was denatured for 10 min at 80°C and reannealed for 30 min at 37°C. Slides were incubated overnight at 37°C. Slide post-hybridization treatments consisted of three washes for 5 min in 50% formamide, 2× SSC pH 7.2–7.4 solution at 45°C, three washes for 5 min in 2× SSC at 45°C, one immersion in 4× SSC, 0.1% Tween 20 at room temperature, one incubation for 30 min with blocking buffer (4× SCC, 4 mg/ml BSA, 0.1% Tween-20) at 37°C, and one incubation for 1 h with anti-digoxigenin-FITC (1:10, Millipore). RNA FISH was then followed by immunostaining with an anti-HORMAD1 antibody (Abcam) at 1:50 dilution. Cells were examined on an Olympus IX70 inverted microscope. Images were captured using a computer-assisted (DeltaVision) CCD camera (Photometrics). Pachytene cells were defined based on continuous HORMAD1 staining along the X- and Y-chromosome axes.

SPO11-oligonucleotide complex detection and western blotting

Testis extract preparation, immunoprecipitation, SPO11-oligonucleotide detection and western blot analysis were performed essentially as previously described[58]. Briefly, SPO11-oligonucleotide complexes and free SPO11 were isolated from testis lysates by two rounds of immunoprecipitation with an anti-SPO11 monoclonal antibody (Spo11-180) on Protein A-agarose beads (Sigma). SPO11-oligonucleotide complexes were labeled with [α-^{32}P] dCTP using terminal deoxynucleotidyl transferase (Fisher), released by boiling in Laemmli buffer and fractionated by SDS-PAGE. The electrophoresed products were transferred onto polyvinylidene fluoride (PVDF) membrane. Radiolabeled species were detected using Fuji phosphor screens and quantified with ImageGauge software. For western blot analysis, the membrane was probed with the SPO11 antibody at 1:2000 dilution.

***In vivo* drug administration**

AZ20 (Selleckchem) compound dissolved in 10% DMSO/40% propylene glycol/50% water was administered orally to adult wild-type males at a single daily dose of 50 mg/kg for 3 or 7 consecutive days or to *Spo11*$^{-/-}$ males for 7 days. Control animals were administrated with the same volume of vehicle solution. Animals were euthanized 24 h after the treatment ended.

Neonatal testis organ culture

Five days *post partum* (dpp) mouse testes were cultured as previously described[59]. Briefly, 1.5% agarose gel cubes were placed in a 6-well plate and pre-soaked overnight in culture medium (10% KSR (Invitrogen), 1% Antibiotic-Antimycotic 100x (Gibco), 0.37% sodium bicarbonate in α-MEM (Invitrogen)) in a culture incubator supplied with 5% CO_2 in air and maintained at 34°C. On the day of the culture, medium from the 6-well plates was removed and replaced with fresh culture medium. Testis fragments from 5 dpp mice were placed on top of the agarose cubes and incubated for 7 days with 5% CO_2 in air and 34°C. Samples were then treated with 0.2 µM, 1 µM or 5 µM AZ20, 1 µM PF-477736 or 1 µM LY2603618 (all drugs from Selleckchem) dissolved in DMSO (Sigma). Control samples were treated with equivalent volumes of DMSO used for each inhibitor concentration. Testis fragments were incubated with 5% CO_2 in air at 34°C for 7 more days. Meiotic spreads from cultured testis fragments were

performed at day 0, 7 or 14 of culture. Surface spreads were immunostained to analyze meiotic progression and recombination.

Image processing and data analysis

Microscopy analysis and image acquisition were performed using a Zeiss Axioskop microscope connected with a ProgRes Jenoptik camera. Images were captured using ProgRes CapturePro software and were processed using Photoshop and ImageJ to quantify fluorescence intensity and chromosome axes length and/or MicroMeasure version 3.3 to analyze MLH1 focus position and axis length, as previously described[19].

FIGURE LEGENDS

Figure 1. At late-prophase stages, Seckel mouse spermatocytes exhibit more γH2AX patches than wild-type cells. (**a**) RT-PCR using primers that anneal to *Atr* exons 8 and 10. $Atr^{S/S}$ testis exhibits two main RT-PCR products, one corresponding to full-length *Atr* (FL *Atr*, 477 bp), which is substantially reduced, and another corresponding to *Atr* lacking exon 9 (ΔE9 *Atr*, 284 bp). Asterisk denotes RT-PCR product resulting from the use of a cryptic splice donor site[16]. RT-PCR for *β Actin* is also provided as a control. (**b**) Percentage of cells exhibiting ATR staining extended to X and Y chromatin or confined to the X and Y chromosome axes. Columns and lines indicate the mean and standard deviation (SD). Images show ATR straining on the sex body in $Atr^{+/+}$ and $Atr^{S/S}$ pachytene spermatocytes. Images were captured with the same exposure time. Scale bar represents 2 μm. (**c**) Quantification of the intensity of γH2AX staining on the sex body in arbitrary units (a.u.). Horizontal black lines denote the means. Images show representative sex bodies from $Atr^{+/+}$ and $Atr^{S/S}$ pachytene spermatocytes immunostained against γH2AX. Images were captured with the same exposure time. Scale bar represents 2 μm. Representative images of $Atr^{+/+}$ (**d**) and $Atr^{S/S}$ (**e**) spermatocytes at different stages of meiotic prophase immunostained against SYCP3, γH2AX, and H1T. Scale bars represent 10 μm. Numbers represent the mean ± SD of γH2AX patches found in each stage and genotype. N denotes the number of cells analyzed. H1T incorporation marks spermatocytes after mid-pachynema[60]. Arrowheads indicate examples of aberrant autosomal γH2AX patches in $Atr^{S/S}$ spermatocytes. The differences between controls and $Atr^{S/S}$ for γH2AX patch numbers at late pachynema and diplonema were statistically significant (p=0.0001 and p=0.0007, respectively, t test).

Figure 2. Normal DSB formation but altered numbers of RAD51, DMC1 and RPA foci in $Atr^{S/S}$ spermatocytes. (**a–c**) Left panels, quantification of total foci per spermatocyte for RAD51 (a), DMC1 (b), or RPA (c) at the indicated stages. Each point is the focus count for a single cell. Horizontal lines denote the mean. Right panels, representative images of spermatocytes stained for the indicated proteins. Scale bar represents 10 μm. All p values are from t test pairwise comparisons; no p value is stated if the comparison was not statistically significant ($p > 0.05$). (**d**) Quantification of SPO11-oligonucleotide complexes. A representative experiment is shown. Anti-SPO11 immunoprecipitates from two testes of each genotype were labeled with terminal transferase and [α-^{32}P]-dCTP, resolved by SDS-PAGE, and detected by autoradiography (top) and western blotting (bottom). Vertical line indicates the signal from SPO11-oligonucleotide complexes; asterisk indicates non-specific signal from the labeling reaction; positions of the two major SPO11 splicing isoforms, α and β are shown; and arrowheads denote the migration position of immunoglobulin heavy chain. SPO11-oligonucleotide signal and testis weights are indicated (mean ± SD). Note that $Atr^{S/S}$ testes express both SPO11α and SPO11β, unlike mutants that experience arrested meiotic progression and lack SPO11β as a consequence[35].

Figure 3. Crossing over in wild-type and $Atr^{S/S}$ spermatocytes. (**a**) Left panels, representative images of pachytene-stage spermatocytes immunostained against SYCP3 and MLH1. Scale bar represents 10 μm and applies to all images. A bivalent lacking an MLH1 focus in the $Atr^{S/S}$ spermatocyte (white box) is magnified in the inset. Right panel, quantification of autosomal MLH1 foci at pachynema. Horizontal black lines denote the means. $Atr^{S/S}$ and control were compared by Mann–Whitney test. (**b**) Proportion of bivalents without an MLH1 focus. N=1520 (mutant) or 1653 (control); p value is from Fisher's exact test. (**c**) Left, representative images of diplotene spermatocytes immunostained against SYCP3. Achiasmate bivalents (white boxes) are magnified in the insets. Right, percentage of achiasmate bivalents at late diplonema from $Atr^{+/+}$ (N=798) and $Atr^{S/S}$ (N=912) spermatocytes (p=0.84, Fisher's exact test). (**d**)

Cumulative frequency plots comparing MLH1 focus distribution along autosomal bivalents from pachytene *Atr*$^{+/+}$ and *Atr*$^{S/S}$ spermatocytes. MLH1 focus distributions were similar between *Atr*$^{+/+}$ (N=924) and *Atr*$^{S/S}$ (N=932). Distributions in SCs presenting one MLH1 focus from *Atr*$^{+/+}$ (N=581) and *Atr*$^{S/S}$ (N=601) and in SCs presenting two MLH1 foci from *Atr*$^{+/+}$ (N=350) and *Atr*$^{S/S}$ (N=369) spermatocytes were also indistinguishable (Kolgomorov–Smirnov (KS) test). (**e**) MLH1 interfocal distances measured in SCs containing two MLH1 foci expressed as a percentage of SC length. Data were fitted to the gamma distribution to measure the strength of interference denoted by the shape parameter (ν)[32].

Figure 4. *In vivo* inhibition of ATR kinase affects prophase progression and markers of homologous recombination. (**a**) Percentage of SYCP3-positive cells from mouse testes treated 3 or 7 days with DMSO (N=2057 and N=986 cells, respectively) or AZ20 (N=2063 and 936 cells, respectively). P value is from Fisher's exact test. (**b**) Percentage of spermatocytes at different prophase stages in 3 and 7 days DMSO- (N=2035 and N=600) and AZ20-treated mice (N=2091 and N=600 cells, respectively). P value is from G test. (**c**) Percentage of pachytene cells exhibiting unsynapsed XY chromosomes in DMSO- (N=472) and AZ20-treated spermatocytes (N=426). P value is from Fisher's exact test. (**d**) Representative images of DMSO- and a AZ20-treated pachytene spermatocytes stained for SYCP3 and γH2AX. Note the presence of a sex body over the XY chromosomes in the control, but not in the AZ20-treated cell. (**e**) RAD51 and RPA foci per spermatocyte at the indicated stages in DMSO- and AZ20-treated mice. Horizontal lines denote the means. P values are from t tests. (**f**) Proportion of tubule sections with 0, 1–4, or >4 TUNEL-positive cells from mice treated with DMSO or AZ20. P value is from t test. Scale bar represents 40 µm. (**g**) Autosomal MLH1 foci in pachytene spermatocytes after 7 days of DMSO or AZ20 treatment. Horizontal black lines denote the means. P value is from a Mann–Whitney test. Images show pachytene spermatocytes immunostained for SYCP3 and MLH1. Scale bars represent 10 µm. (**h**) Cumulative frequency plots comparing MLH1 focus distribution along autosomal bivalents from pachytene spermatocytes after 7 days of DMSO or AZ20 treatment. MLH1 focus distribution along all autosomal bivalents was similar between DMSO (N=320) and AZ20 (N=233) treatments. In SCs presenting one MLH1 focus from DMSO- (N=204) and AZ20- (N=138) treated mice or two MLH1 foci from DMSO- (N=116) and AZ20- (N=94) treated mice, MLH1 focus location was also indistinguishable (KS test). (**i**) MLH1 interfocal distances expressed as a percentage of SC length from autosomal bivalents containing two MLH1 foci. Shape parameters (ν) from gamma distribution are shown³²³²³¹³¹(de Boer et al., 2006).

Figure 5. ATR and CHK1 inhibitors block meiotic recombination and prophase progression *in vitro*. (**a**) Percentage of SYCP3-positive cells present in untreated testis fragments at 0, 7 and 14 days of culture (D0, D7 and D14, respectively). Columns and lines indicate the mean and SD in all bar graphs. (**b**) Percentage of spermatocytes at the indicated stages of prophase in untreated testis fragments. (**c**) Proportion of SYCP3-positive cells at D14 in testis fragments treated with the indicated dosages of AZ20, PF-477736, or LY2603618, and their respective DMSO controls. P values are from Fisher's exact tests. (**d**) Proportion of spermatocytes at different stages of meiotic prophase at D14 of culture. P values are from G tests. (**e**) Representative images of spermatocytes from testes treated with DMSO3 or 5 µM AZ20 showing progression of meiotic prophase, followed by staining for SYCP3 and γH2AX. (**f**) RAD51 foci at the indicated stages from D14 cultures. (Color code key is in panel (**i**).) In this and other graphs of focus counts, horizontal lines denote the means and p values are from pairwise t tests. (**g-h**) Representative spermatocytes from cultured samples stained for SYCP3 and either RAD51 (**g**) or DMC1 (**h**). (**i**) RPA foci in cultured spermatocytes. (**j**) RAD51 foci per

spermatocyte from control and PF-477736- or LY2603618-treated samples. (**k**) Representative images of spermatocytes from D14 cultures treated with DMSO or 1 µM PF-477736 and immunostained for SYCP3 and RAD51. Data presented for each culture condition correspond to at least two experiments performed using different samples. Scale bars in all micrographs represent 10 µm.

Figure 6. ATR function is required for the accumulation of recombination markers on unsynapsed axes. (**a**) RAD51 focus density along the entire measurable X-chromosome axis. Horizontal black lines denote the means. P values are from t tests. (**b**) Representative images of late zygotene spermatocytes. Images show overlays of immunofluorescence against SYCP3 and RAD51 with fluorescence *in situ* hybridization (FISH) for the X-PAR boundary. Scale bar represents 10 µm. Inset images show RAD51 foci on the measurable X-chromosome axis. (**c**) RPA focus density on the measurable X chromosome. (**d**) Images of early zygotene spermatocytes showing immunofluorescence against SYCP3 and RPA, overlaid with FISH for X-PAR boundary. Inset images show RPA foci on the measurable X-chromosome axis. (**e**) RPA focus numbers present on unsynapsed axes at D14 from spermatocytes cultured *in vitro*.

Supplementary figure 1. Reduction of ATR expression in $Atr^{S/S}$ testes leads to abnormal sex-body formation. (**a**) Seminiferous tubule cross-sections from $Atr^{+/+}$ and $Atr^{S/S}$ stained with PAS-hematoxylin contain multiple spermatogenic stages, from spermatogonial stem cells at the base of the tubule to elongated spermatids at the lumen. (**bi**) Representative images from $Atr^{+/+}$ and $Atr^{S/S}$ spermatocytes immunostained for SYCP3 and SYCP1. Scale bar represents 10 µm. $Atr^{S/S}$ spermatocytes complete autosomal synapsis, however note the presence of unsynapsed X and Y chromosomes in $Atr^{S/S}$ spermatocytes at pachynema (white box). (**bii**) Magnified images of sex chromosomes at pachynema (white boxes). In control spermatocytes, sex-chromosome synapsis is demonstrated by the presence of SYCP1 in the PAR (arrow). $Atr^{S/S}$ spermatocytes exhibit unaligned sex chromosomes presenting only SYCP3 staining. (**c**) Percentages of cells present at different prophase stages from the indicated genotypes. Columns and lines indicate the mean and SD. Similar proportions of spermatocytes were found at each stage of meiotic prophase in $Atr^{+/+}$ and $Atr^{S/S}$ (N=402 and N=370 respectively, p=0.62, G test). (**d**) Quantification of the intensity of MDC1 and SUMO-1 staining on the sex body in arbitrary units (a.u.). Horizontal black lines denote the means. Images show representative sex bodies from $Atr^{+/+}$ and $Atr^{S/S}$ pachytene spermatocytes immunostained for MDC1 or SUMO-1. Images were captured with the same exposure time. Scale bar represents 2 µm. (**e**) Percentage of cells exhibiting *Zfx* RNA FISH signals in $Atr^{+/+}$ (5%, N=95) and $Atr^{S/S}$ (4%, N=48, p=1.0, Fisher's exact test). (**f**) Representative early-pachytene spermatocytes stained for HORMAD1, which is confined to sex chromosomes (arrows) at early pachynema, overlayed with RNA FISH for the X-linked gene *Zfx* and DAPI. Note that *Zfx* was not expressed in the pachytene spermatocytes shown, indicative of proper MSCI in both genotypes. (One HORMAD1-negative cell expressing the X-linked gene is shown (arrowhead)).

Supplementary figure 2. *In vivo* inhibition of ATR inhibits SC elongation in $Spo11^{-/-}$ spermatocytes. (**a**) Representative images from $Spo11^{-/-}$ spermatocytes treated with 5 µM AZ20 or the equivalent volume of DMSO for 7 days. Scale bar represents 10 µm. (**b–c**) Quantification of the number (**b**) and the length (**c**) of SC stretches. Horizontal lines denote the means. P values are from t tests.

Supplementary table 1. Average number of recombination foci present in spermatocytes at different stages of meiotic prophase from the indicated genotypes.

		Early leptonema	Late leptonema	Early zygonema	Late zygonema	Pachynema	Diplonema
RAD51	*Atr*$^{+/+}$	187.6 ± 66.4, N=22	165.8 ± 48.5, N=12	162.0 ± 42.6, N=15	78.5 ± 82.8, N=38	21.0 ± 14.8, N=61	13.1 ± 11.4, N=15
	Atr$^{S/S}$	120.8 ± 62.0, N=12	151.4 ± 47.7, N=16	144.5 ± 39.2, N=53	82.8 ± 27.24, N=79	29.9 ± 16.2, N=104	11.9 ± 8.4, N=29
DMC1	*Atr*$^{+/+}$	181.0 ± 90.1, N=12	163.1 ± 40.2, N=9	118.5 ± 31.6, N=32	65.81 ± 22.6, N=58	19.3 ± 16.0, N=77	2.07 ± 2.7, N=28
	Atr$^{S/S}$	118.3 ± 38.6, N=22	95.2 ± 27.7, N=18	100.3 ± 33.5, N=27	57.73 ± 17.5, N=56	31.2 ± 17.2, N=80	3.2 ± 3.2, N=13
RPA	*Atr*$^{+/+}$	156.8 ± 45.4, N=15	152.5 ± 28.16, N=12	178.2 ± 28.6, N=18	121.4 ± 29.1, N=42	62.2 ± 36.2, N=58	4.9 ± 4.8, N=18
	Atr$^{S/S}$	193.0 ± 52.5, N=17	156.8 ± 22.9, N=19	132.9 ± 33.6, N=15	113.1 ± 15.6, N=41	56.8 ± 31.7, N=79	3.2 ± 3.0, N=24

Mean, standard deviation and total number of cells counted (N) are shown.

Supplementary table 2. Average number of recombination foci in spermatocytes from mice treated with ATRi or the control vehicle DMSO at the indicated stages of prophase.

		Early leptonema	Late leptonema	Early zygonema	Late zygonema
RAD51	DMSO treatment	173.8 ± 47.3, N=16	184.6 ± 36.0, N=26	153.3 ± 32.31, N=31	91.41 ± 27.5, N=41
	AZ20 treatment	129.1 ± 49.0, N=19	131.2 ± 51.9, N=35	131.5 ± 33.7, N=64	86.2 ± 44.4, N=40
RPA	DMSO treatment	199.1 ± 30.3, N=21	177.2 ± 35.5, N=24	182.8 ± 52.5, N=34	131.5 ± 35.5, N=31
	AZ20 treatment	238.2 ± 56.6, N=20	155.6 ± 33.5, N=20	127.6 ± 31.1, N=33	97.74 ± 26.5, N=38

Mean, standard deviation and total number of cells counted (N) are shown.

Supplementary table 3. Average percentage of spermatocytes and proportions of cells in meiotic prophase stages in cultured samples.

		% Spermatocytes	% Leptonema	% Zygonema	% Pachynema	N
Untreated	D0	0.70 ± 1.1, N=709	100.0 ± 0.0	–	–	3
	D7	11.5 ± 5.4, N=1032	76.1 ± 10.5	23.3 ± 9.7	0.65 ± 1.0	324
	D14	15.1 ± 2.9, N=1214	20.0 ± 3.8	54.5 ± 15.3	25.6 ± 12.7	490
AZ20	DMSO1	14.3 ± 5.6, N=825	24.6 ± 5.3	45.1 ± 4.1	30.3 ± 7.9	492
	0.2 µM	13.7 ± 5.2, N=860	23.9 ± 3.7	52.4 ± 10.2	23.7 ± 6.5	280
	DMSO2	19.5 ± 3.6, N=829	28.0 ± 2.5	47.7 ± 5.3	24.3 ± 2.8	218
	1 µM	8.0 ± 2.9, N=829	32.7 ± 2.9	67.3 ± 2.9	0	486
	DMSO3	11.5 ± 1.6, N=844	27.8 ± 10.2	53.1 ± 3.6	19.1 ± 10.8	400
	5 µM	1.4 ± 0.1, N=818	54.1 ± 16.0	45.9 ± 16.0	0	194
CHKi	DMSO	9.5 ± 1.5, N=563	27.4 ± 5.7	53.4 ± 7.4	18.8 ± 1.7	189
	1 µM PF-477736	2.6 ± 0.1, N=386	38.3 ± 2.4	61.7 ± 2.4	0	192
	1 µM LY2603618	4.4 ± 2.0, N=397	38.3 ± 7.0	61.8 ± 7.0	0	133

Mean, standard deviation and total number of cells counted (N) are shown.

Supplementary table 4. Average number of recombination foci in cultured spermatocytes at the indicated stages of prophase.

		Early leptonema	Late leptonema	Early zygonema	Late zygonema
RAD51	D14 – untreated	157.7 ± 25.0, N=6	137.8 ± 36.1, N=21	111.2 ± 24.8, N=39	63.0 ± 26.8, N=24
	DMSO3-AZ20 treatment	121.7 ± 32.0, N=7	141.6 ± 37.0, N=16	112.7 ± 34.2, N=27	61.5 ± 17.3, N=28
	5 µM AZ20	21.8 ± 21.3, N=16	16.6 ± 16.6, N=14	13.9 ± 14.6, N=42	8.9 ± 11.0, N=21
	DMSO-CHK1i treatment	82.2 ± 49.9, N=25	126.4 ± 46.7, N=37	136.9 ± 39.8, N=19	94.6 ± 32.3, N=21
	1 µM PF-477736	23.5 ± 18.5, N=17	41.4 ± 22.7, N=37	43.9 ± 29.6, N=24	31.5 ± 17.9, N=22
	1 µM LY2603618	23.6 ± 16.2, N=22	46.2 ± 39.8, N=28	54.2 ± 35.2, N=24	48.2 ± 19.9, N=12
RPA	D14 – untreated	152.3 ± 18.46, N=13	150.6 ± 24.7, N=11	147.4 ± 44.2, N=16	130.5 ± 31.5, N=12
	DMSO3-AZ20 treatment	154.0 ± 33.2, N=13	114.3 ± 21.4, N=12	136.6 ± 35.1, N=16	96.76 ± 30.9, N=17
	5 µM AZ20	200.2 ± 80.6, N=17	149.9 ± 33.9, N=11	133.7 ± 58.2, N=12	81.4 ± 11.6, N=5

Mean, standard deviation and total number of cells counted (N) are shown.

Figure 1

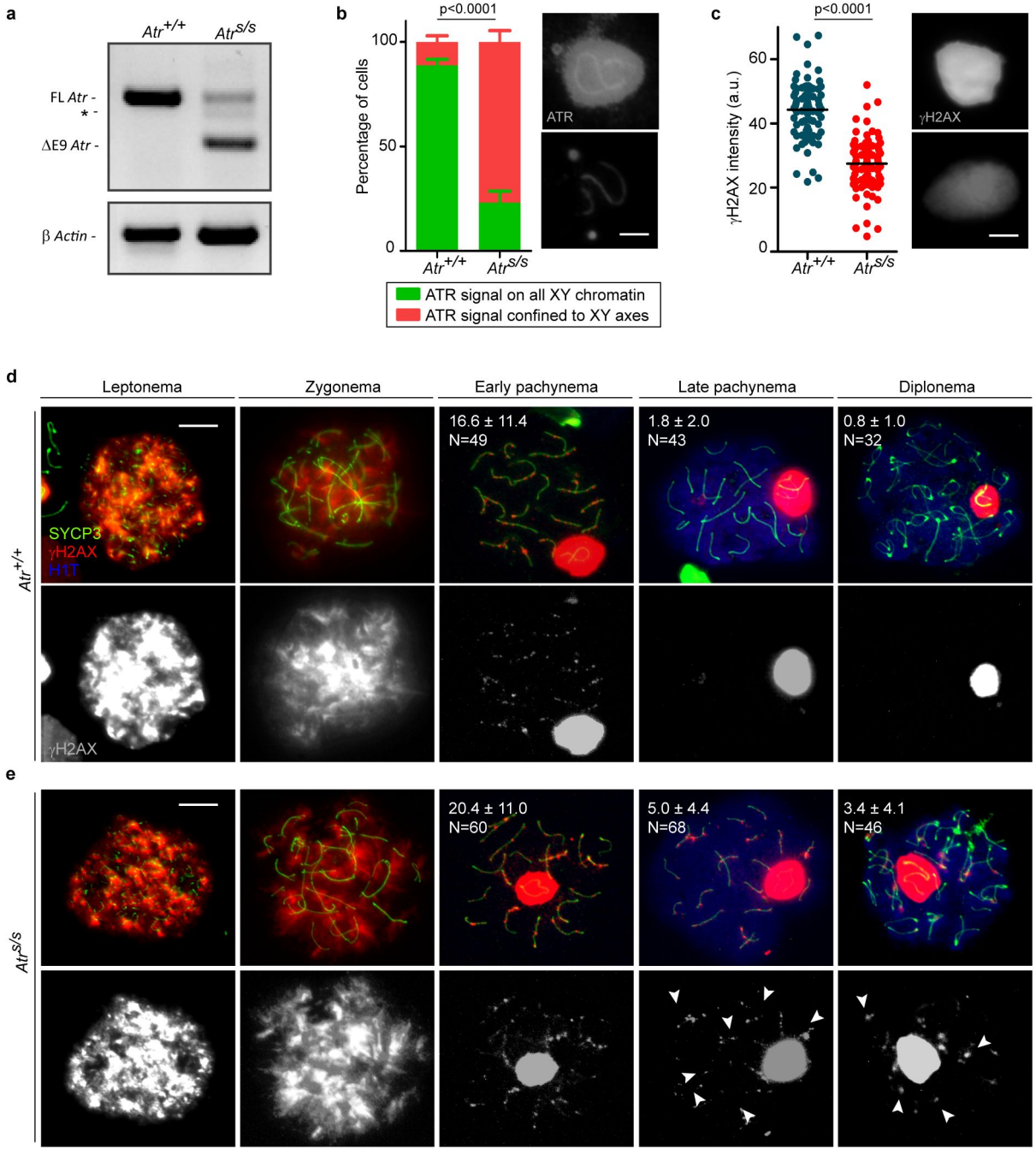

Figure 2

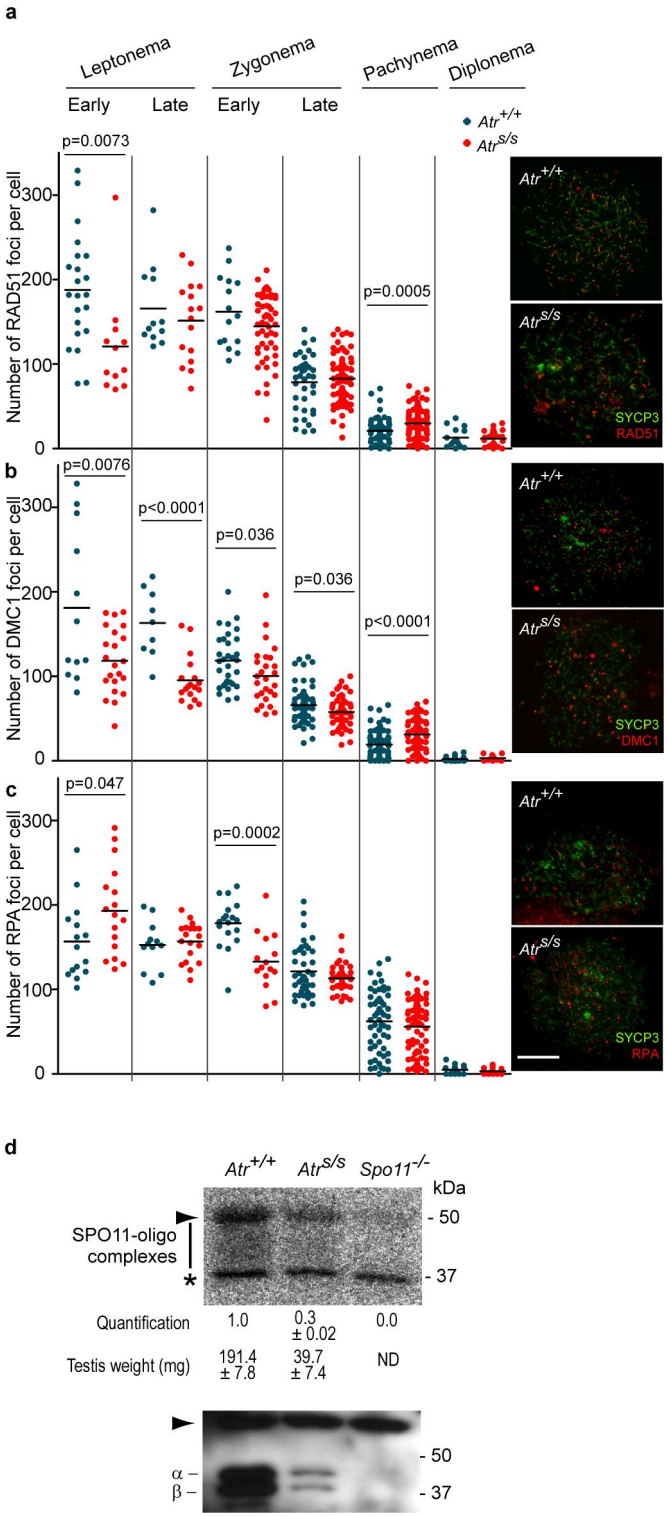

Figure 3

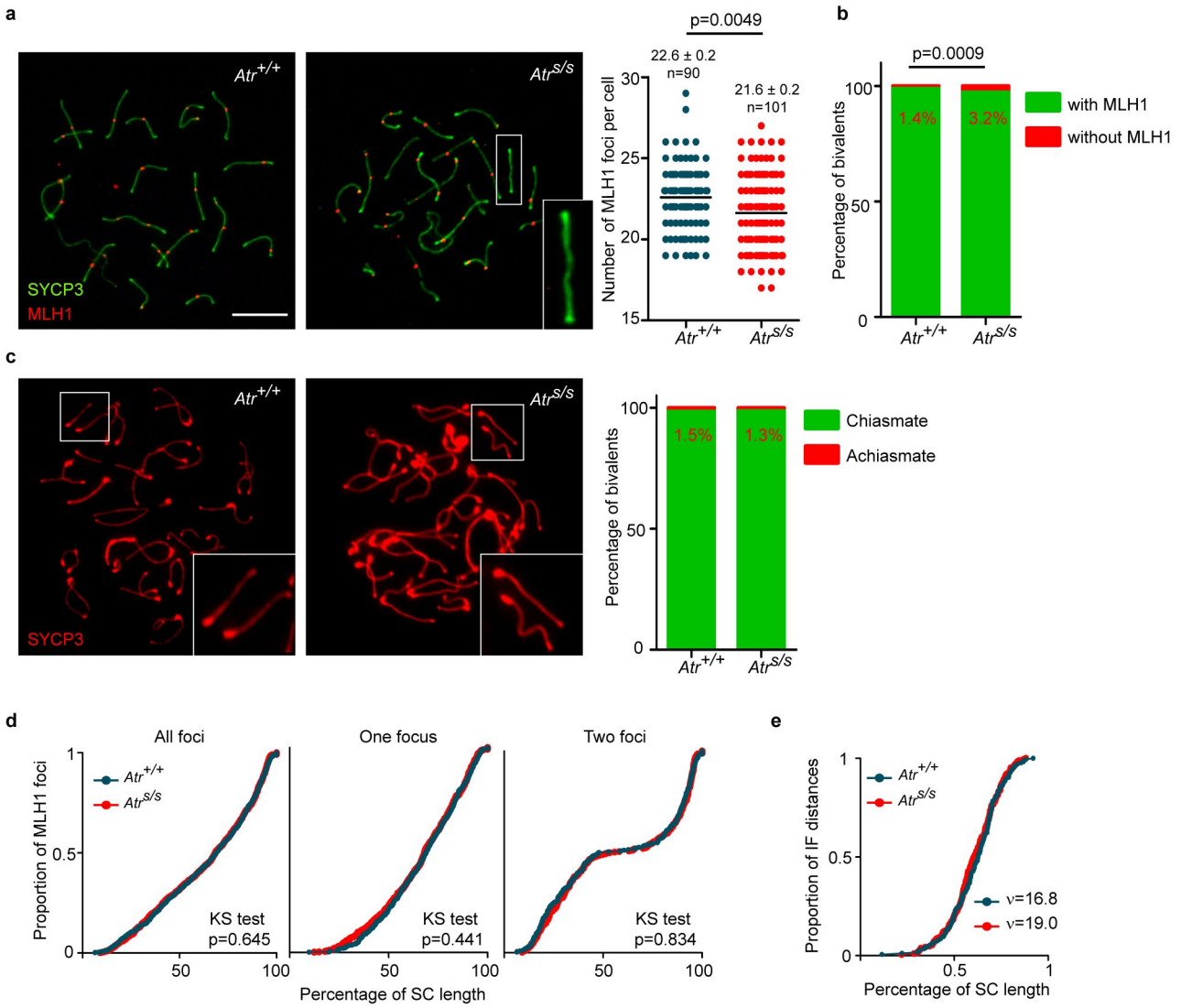

Figure 4

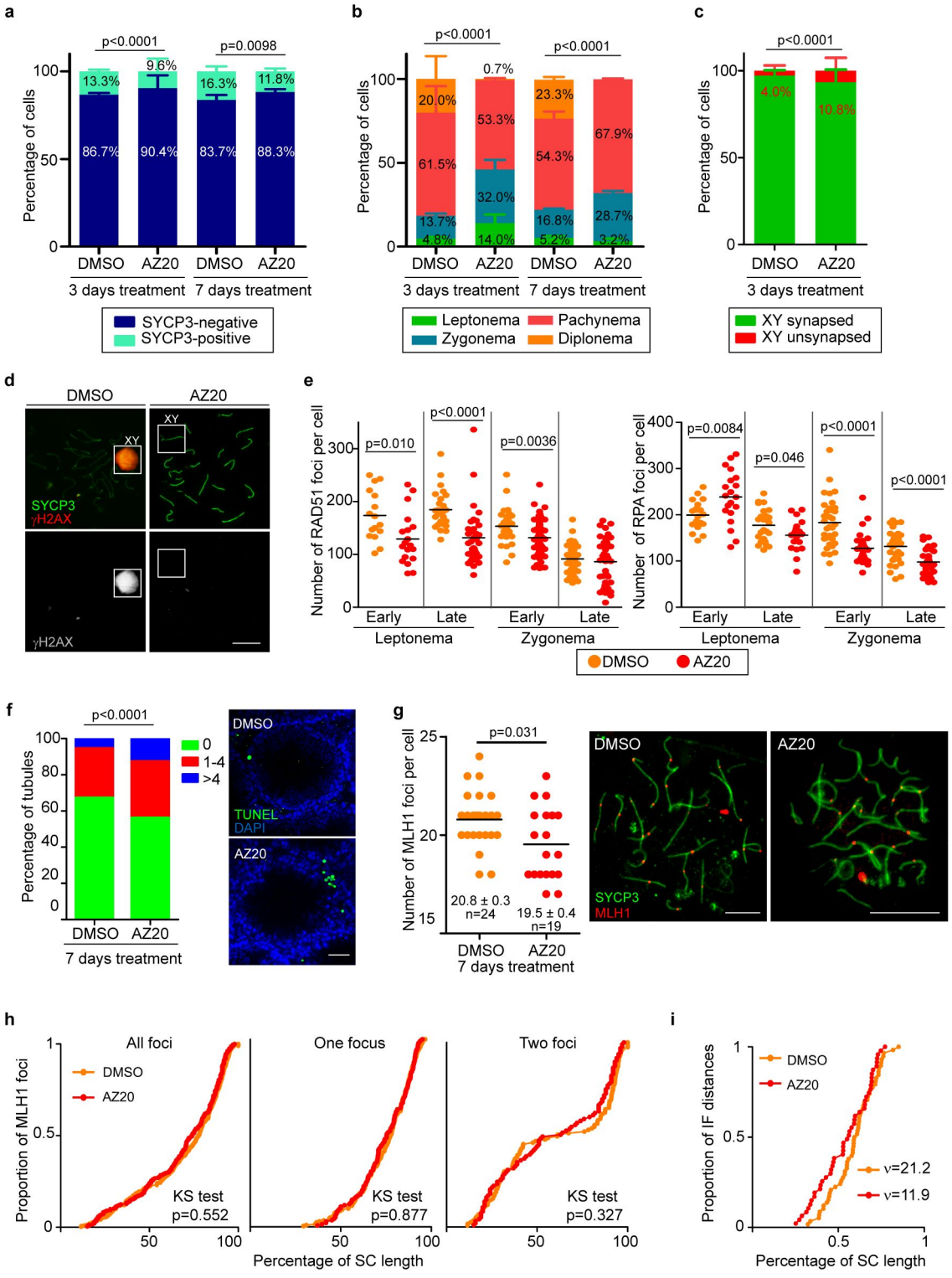

Figure 5

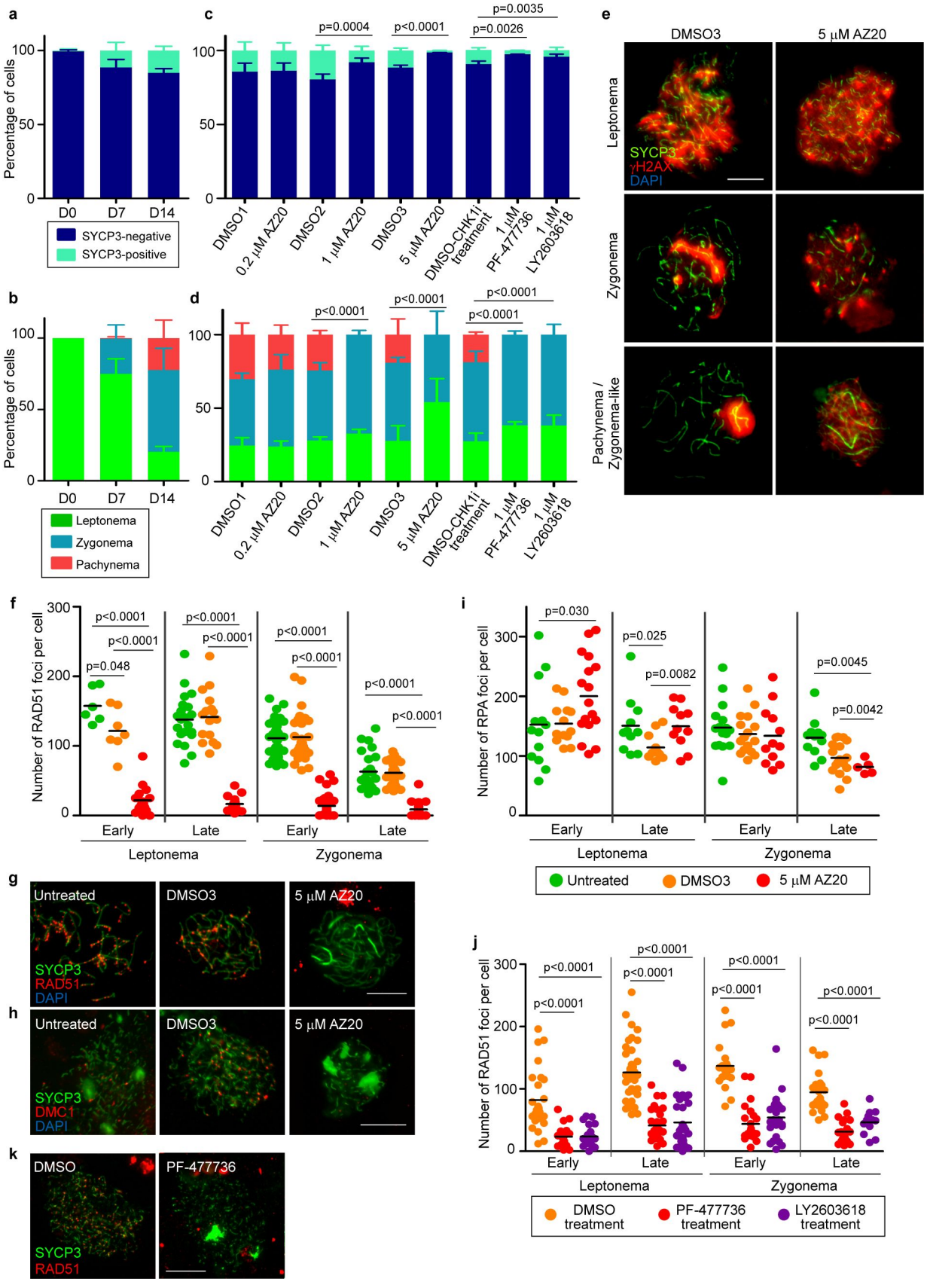

Figure 6

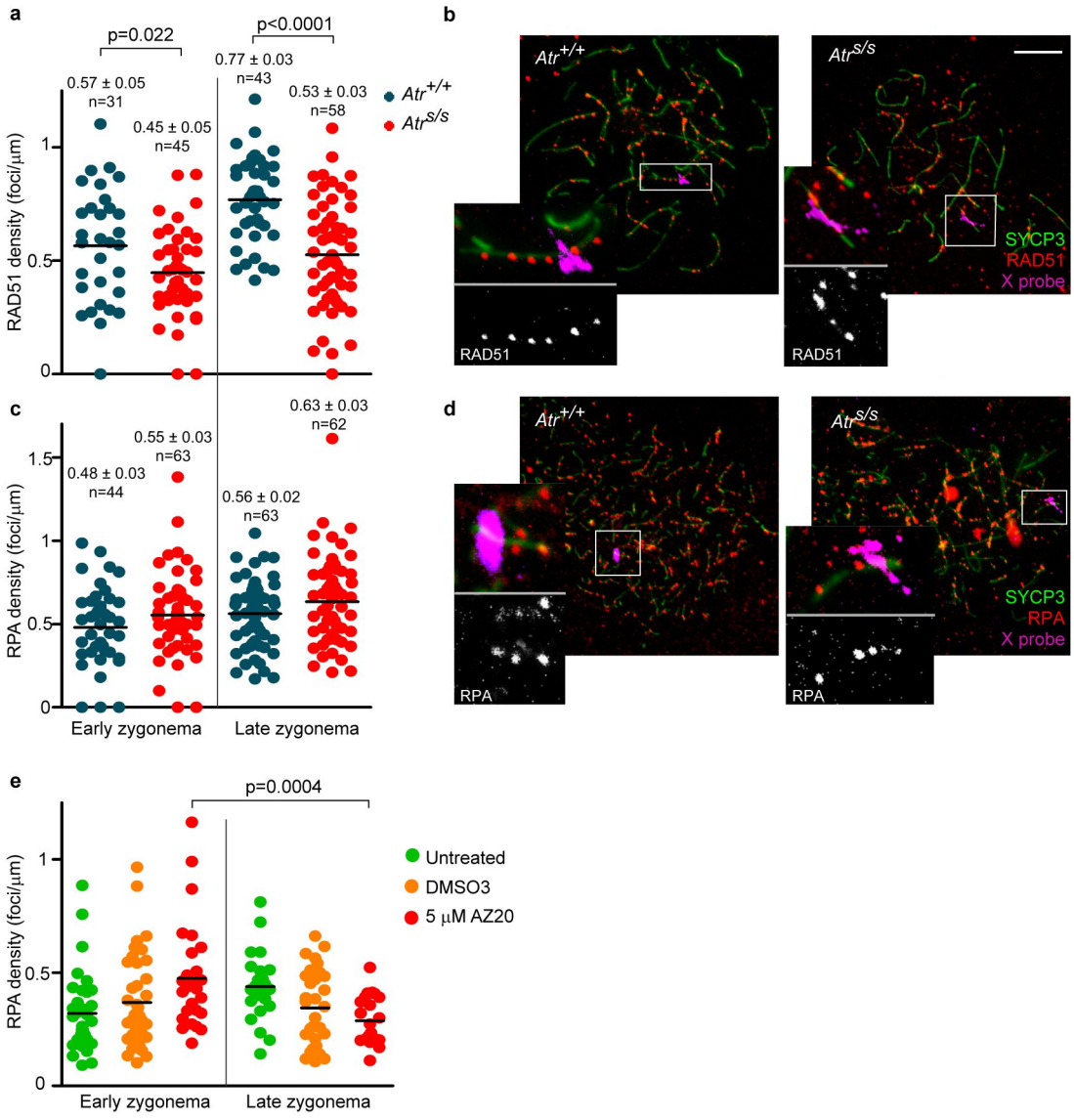

Supplementary Figure 1

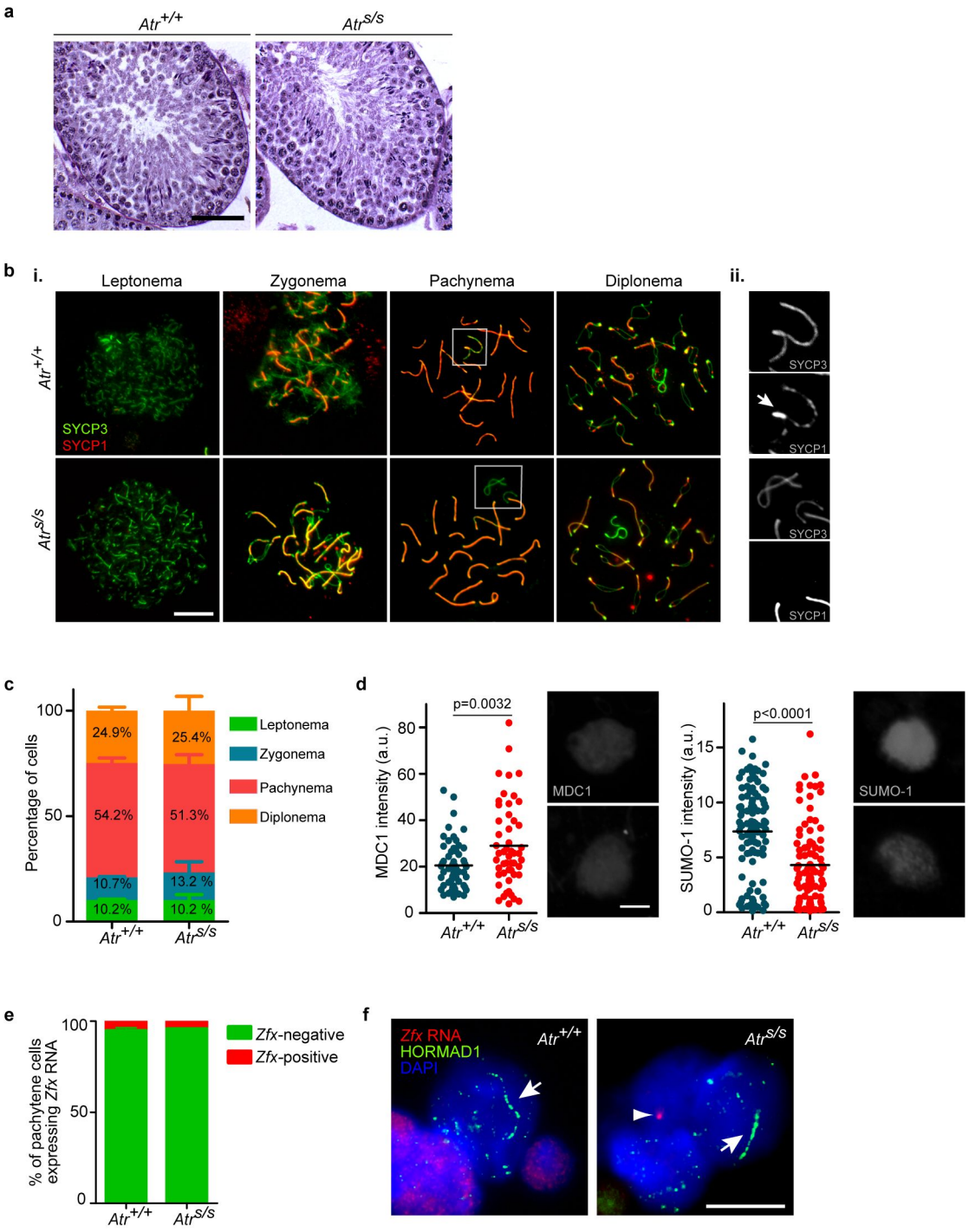

Supplementary Figure 2